Interfacial fracture behavior and adhesive strength in tensile and shear loading of SiC-PyC-SiC composites by micro-scale specimens

8 authors, including:

Johannes Ast
Friedrich-Alexander-University of Erlangen-Nürnberg
20 PUBLICATIONS **820** CITATIONS

SEE PROFILE

Chunhua Tian
Empa - Swiss Federal Laboratories for Materials Science and Technology
19 PUBLICATIONS **129** CITATIONS

SEE PROFILE

Nadia Rohbeck
Empa - Swiss Federal Laboratories for Materials Science and Technology
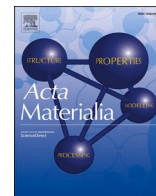**28** PUBLICATIONS **398** CITATIONS

SEE PROFILE

Daniele Casari
Empa - Swiss Federal Laboratories for Materials Science and Technology
24 PUBLICATIONS **401** CITATIONS

SEE PROFILE

Full length article

Interfacial fracture behavior and adhesive strength in tensile and shear loading of SiC-PyC-SiC composites by micro-scale specimens

J. Ast [a,b,1], C. Tian [c,1,*], P. Herre [d], N. Rohbeck [c], D. Casari [c], J. Michler [c], S.H. Christiansen [a,d,e], J.J. Schwiedrzik [c,*]

[a] *Fraunhofer IKTS, Fraunhofer Institute for Ceramic Technologies and Systems, Forchheim, Germany*
[b] *Current affiliation: University Grenoble Alpes, CEA, LITEN, Grenoble, France*
[c] *Empa Swiss Federal Laboratory for Material Science and Technology, Laboratory of Mechanics of Materials and Nanostructures, Thun, Switzerland*
[d] *Innovation Institute for Nanotechnology and Correlative Microscopy, Forchheim, Germany*
[e] *Helmholtz Center for Materials and Energy, Berlin, Germany*

ARTICLE INFO

ABSTRACT

Micromechanical tests were performed to understand the local fracture behavior and adhesive strength of a fiber-reinforced ceramic matrix composite (silicon carbide fiber reinforced silicon carbide matrix with the pyrolytic interphase in between, $SiC_{fiber}/PyC/SiC_{matrix}$) and to determine the mode-dependent interfacial fracture toughness. A combined approach of pico-second laser ablation and focused ion beam milling was used to fabricate notched and unnotched micro-cantilever and in-plane micro-shear specimens for mode I and II testing. Due to the complexity of the sandwich system, finite element simulations were implemented, which took into account the elastic heterogeneity, the influence of PyC thickness, Young's modulus and beam thickness. This allowed us to obtain mode-specific geometry functions and to increase the accuracy of the obtained stress intensity factor. In all cases, a failure at the SiC_{fiber}/PyC interface was observed. While straight through notched specimens exhibit a systematic overestimation of fracture toughness due to the less accurate alignment of notch root and PyC layer, curved notched specimens show a very low interfacial fracture toughness of 0.24 ± 0.02 MPa$\sqrt{m}$ and 0.17 ± 0.06 MPa$\sqrt{m}$ in mode I and mode II, respectively. Combined with tests on unnotched specimens, a critical flaw size for the present microstructure of the PyC phase of ca. 21 nm was identified. The data underlines the important role of the PyC interlayer in damage resistant ceramic composites and the developed methodology, which can be used for systematic studies of their properties as a function of process, geometry, and boundary conditions.

1. Introduction

Ceramic fiber matrix composites (CFMC) are being considered for a range of structural components due to their variety and flexibility in shape and design, their high temperature mechanical performance as well as low weight [1–5]. The enormous progress made recently in fabricating high-quality, pure silicon carbide (SiC) fibers enables a large-scale production that is economically viable. With the concomitant reduction in cost, a widespread commercial application of fully ceramic SiC fiber-SiC matrix composite materials has become possible. In contrast to monolithic ceramic components that can fail by the propagation of one single crack, CFMC are designed in such a way that cracks

are deflected upon encountering a second phase [6]. Several mechanisms (e.g. debonding of fibers, crack bridging) help to dissipate the fracture energy and thus prevent a rapid complete failure as seen in conventionally sintered ceramic parts [7,8]. Still, CMCs share the same physical properties as the ceramics they are based on. Among all CFMC competitors, the SiC-based systems (SiC_f/SiC_m) stand out due to their high strength at high temperatures, good inertness to chemical attack and low specific weight of 3.2 g/cm³. These advantages have made SiC-based CFMCs a prime candidate to replace the nickel-based super-alloys in turbine blades in future aero engines [9,10].

In addition to its use in the aerospace industry, SiC has demonstrated an excellent performance in a harsh neutron environment within a

number of irradiation studies and has been investigated for different applications in the nuclear reactor [11,12]. Contrary to zircaloy fuel cladding, the current standard in commercial water-cooled nuclear reactors, SiC offers a thermal stability beyond 2000 °C and does not melt. Thus, significant efforts have been made to manufacture fuel cladding tubes consisting of SiC, which form an integral part of the novel accident tolerant design replacing current fuel cladding.

Many common sintering additives for SiC act as a neutron poison and thus the fabrication of SiC fiber-SiC matrix composites for nuclear components relies on processing steps that do not add any impurities [13]. The initial SiC fiber bundles are brought into the correct shape and are subsequently infiltrated by chemical vapor infiltration (CVI) yielding a pure and stoichiometric SiC. In this way, homogeneous tubes of several metres' length can be made that allow to hermetically seal the nuclear fuel in operation.

One important topic in composites deals with the understanding of fracture mechanisms and fracture behavior [14]. The effectiveness of the pyrolytic carbon (PyC) or boron nitride (BN) layer in CFMC is a central key for the ability of the composite to withstand overall failure [15,16]. Fracture across the interlayer and fibers is "desired" since crack deflection leads to energy dissipation in the material. Therefore, a precise local understanding of the interlayer properties as well as its interfaces to fiber and matrix material assessed by micromechanical testing and high resolution imaging are indispensable. Numerous studies emphasize the importance of the determination of local debonding shear strength and fracture toughness analysis. Advantages of the fiber pull-out and push-out techniques are the direct assessment of tribological properties of the interlayer, its classification into cohesive or adhesive type and determination of shear strength [17–23]. A more thorough but generally less statistical approach to overcome disadvantages of the fiber push-out method is achieved by focused ion beam (FIB) produced micropillars [24–26]. These geometries aim at smaller portions of interlayer, which is beneficial for alignment of indentation tips and extraction as well as discussion of physical properties. However, in terms of a fracture mechanical analysis, disadvantages are the irregular size and distribution of flaws along the interface. Upon catastrophic failure of the interface this can lead to significant scatter in data in micropillar experiments, which contain inclined interfaces. To overcome this issue, notched micro-cantilevers with a precise definition of the stress field ahead of the crack tip and double cantilever beams allowing controlled stable crack growth and therefore an assessment of critical fracture energy release rates as a function of crack length have been proposed recently [27,28].

Based on a previous study [29], in which new micro-scale specimen designs are proposed for mode I, II and III fracture testing, we adapt those geometries to test the PyC layer. Microcantilever bending and micro-shear tests are performed to determine the interface debonding strength in mode I and II and to compare this data with fracture tests on the same geometries containing FIB machined notches.

Here, the novelty is the high precision tailoring of curved notches to round SiC fibers with dimensions in the micron regime and their PyC layer of just below 100 nm, as well as the adequate numerical assessment of new geometry functions and stress intensity factor distributions along the curved crack front by means of finite element (FE) simulations. These investigations are performed for mode I (bending) and mode II (shear), allowing a detailed analysis of fracture behavior in terms of fracture initiation and observation of controlled crack propagation at the PyC layer. However, the proposed methodology here is not only applicable to such fiber-based composites, but also acts as a reference for other systems where interfaces and boundaries play a role, for instance, when investigating the fracture property of grain boundaries in polycrystalline materials, of phase boundaries between inclusions/precipitates and matrix as well as of the multilayer laminates with two or more constituents. Our work stresses the significance of a target-tailored testing geometry and also the consideration of elastic mismatch between components, in order to correctly measure the fracture toughness of interfaces and correlate it with microstructural and chemical features.

2. Experimental

2.1. Sample preparation

The SiC composite consists of SiC fibers coated with a carbon interphase and embedded inside a SiC matrix synthesized by CVI. The sample is fabricated in the shape of a thin plate approximately 1 mm in thickness and is provided by General Atomics (San Diego, USA). The exact deposition parameters are specific to the CVI furnace and proprietary, but a general description of the fabrication process can be found in [30]. The thickness of the PyC layer is measured to be 80 ± 20 nm ($N = 30$) by scanning electron microscopy (SEM). A two by two cm piece is cut with a diamond saw. Subsequently, one side is polished flat in order to remove the matrix SiC and expose the fibers that run parallel to the polished side. Diamond particle containing polishing paste with decreasing particle size is used to avoid surface damage.

For further processing, the sample is fixed into a conventional SEM compatible clamping holder using Cu tape and small amounts of conductive Ag paste. A picosecond (ps) pulse Nd:YVO4 laser (CEPHEUS workstation, Photon Energy GmbH, Germany) cutting step perpendicular to the polished surface is performed to remove larger amounts of matrix material close to fiber bundles and to access individual well-embedded fibers. In a previous study on SiC-diamond interfaces this technique has also proven to be efficient and successful [31].

Notched and unnotched micro-cantilever and micro-shear specimens are prepared by focused ion beam (FIB) machining (Tescan Lyra, Czech Republic) using Ga+ ions with 30 kV acceleration voltage. Beam currents in the range of 2–10 nA and below 1 nA are used for coarse milling and final polishing, respectively. For fracture toughness evaluation, both straight through notches (STN) and curved notches (CN) are milled at 60pA at the ~100 nm thick PyC layer and for both geometries. Micro-cantilevers are designed in such a way that their support always consists of the fiber and their long axis of the matrix material with the PyC phase being close to the support. Micro-shear specimens are fabricated in individual fibers in a way that the shear surfaces are located at the PyC phase. Fig. 1 gives an overview of the prepared sample with different specimen types.

Final specimen dimensions for micro-cantilevers and micro-shear specimens can be found in Table 1. It can be seen that, for fracture specimens with STN type, it is requested to have fine dimensions in width B to stay close to the PyC layer. This reduces significantly flexibility of specimen design as compared to the thicker CN specimens. As will be shown in the results chapter, this is crucial in particular for highly brittle materials.

2.2. Microstructure analysis

Transmission electron microscopy investigations (TEM, FEI Titan Themis 200 G3 at 200 kV, probe corrected), were performed on the SiC_fiber/PyC/SiC_matrix sandwich interface, as shown in Fig. 2, to visualize the microstructure, assess the interface properties as well as qualitatively determine the chemical composition. Energy dispersive X-ray spectroscopy (EDS) maps were recorded using the integrated SuperX detector. Using the line intercept method, it was found that the SiC fiber has equiaxed grains with a grain size of 170 ± 23 nm, whereas the SiC matrix features elongated grains with a width of 163 ± 33 nm and a length of 1200 ± 200 nm, as shown in Fig. 2a. The roughness at the SiC_fiber/PyC interface is seemingly larger than at the PyC/SiC_matrix. For an estimation, two parallel red lines approximating the width of the roughness profile are drawn at the SiC_fiber/PyC interface side. The roughness is defined by Rt, the sum of the maximum peak height and the maximum valley depth of a profile within the evaluation length (here the TEM interface shown in Fig. 2a). This way, the roughness at the SiC_fiber/PyC interface is approximated to be 73 nm while at the PyC/
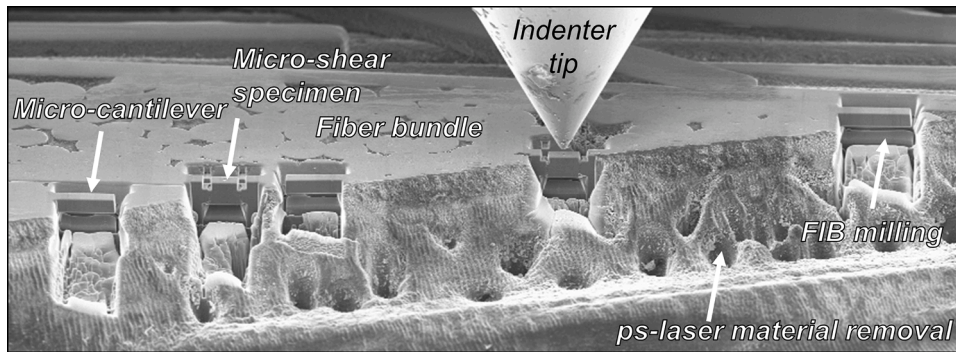
Fig. 1. SE image with inclined view of the specimen surface and edge featuring some of the micro-scale test geometries as prepared by a combination of coarse ps-laser material removal and subsequent FIB milling in the vicinity of individual SiC fibers to test PyC interlayers. For further details on specimen size and shape as well as notch design, the reader is referred to Figs. 6–8.

Table 1
Micro-cantilever and micro-shear specimen dimensions as explained in the following for the two notch types for fracture toughness testing (STN and CN) and the two specimen types without notch (-).

Type	Notch	L/μm	B/μm	W/μm	a/W	$\widetilde{f}$(a/W)	Tests
Micro-cantilever	STN	7.45 ± 1.40	1.86 ± 0.42	2.54 ± 0.43	0.43 ± 0.05	8.73 ± 1.39	8
	CN	15.64 ± 1.06	5.96 ± 0.41	5.16 ± 0.07	0.19 ± 0.01	2.95 ± 0.07	7
	–	8.59 ± 0.49	3.60 ± 0.16	2.93 ± 0.10	–	–	10
Micro-shear specimen	STN	–	1.92 ± 0.17	1.53 ± 0.05	0.35 ± 0.02	1.41 ± 0.05	7
	CN	–	4.62 ± 0.36	2.71 ± 0.14	0.27 ± 0.01	0.93 ± 0.02	7
	–	–	3.44 ± 0.34	3.03 ± 0.10	–	–	10

SiC$_{matrix}$ it is 42 nm.

At a higher magnification, small flaws are occasionally found along the SiC$_{fiber}$/PyC interface (Inset in Fig. 2a and Fig. 2b). This is especially the case where sharper edges/angles are found and the roughness is locally increased as demonstrated in Fig. 2b. In contrary, the PyC/SiC-matrix interface appears defect-free and shows a flaw-less transition from one phase into the other. Noteworthy as well is that the grain boundaries in the SiC fiber are decorated with carbon-rich precipitates as confirmed by the STEM-EDS elemental mapping in Fig. 2c. Fig. 2d displays a high-resolution TEM image, highlighting the amorphous nature of the PyC interlayer and the crystallinity of the SiC material (exemplarily shown for the SiC fiber, see diffraction patterns in Fig. 2d).

2.3. Fracture testing in the SEM

All fracture experiments are performed at room temperature in-situ inside a SEM (Zeiss Auriga workstation) using a displacement-controlled nanoindentation platform (Alemnis AG, Switzerland). For micro-cantilever testing a sphero-conical diamond tip with radius of approximately 1 μm is used to facilitate positioning, avoid alignment issues and reduce sample deformation at the indentation site [32,33]. Depending on specimen thickness and applied loads the sphero-conical or alternatively a flat punch tip with 5 μm diameter are used for notched and unnotched shear experiments. In case of the flat punch tip, the misalignment between tip and sample is always verified to be below 1°

and is thus deemed negligible. Effects of slight indentation tip misalignment in micro-shear experiments are discussed in detail in a previous study [29]. Constantly, low displacement rates of 10 nm/s are applied in all experiments because of the very brittle interfaces leading to low bending and shear strain. The determination of mode I and II stress intensity factors K$_I$ and K$_{II}$, respectively, is based on the following Eqs. (1) and (2):

$$K_I = \frac{FL}{BW^{3/2}} \cdot f_{KI}\left(\frac{a}{W}\right) \tag{1}$$

$$K_{II} = \frac{F}{2B\sqrt{W}} \cdot f_{KII}\left(\frac{a}{W}\right) \tag{2}$$

Here, F is the applied load, L the distance from the notch to the point of loading measured along the edge of the specimen, B the specimen width, a the crack length, and W the specimen height. Geometric dimensions are illustrated in Fig. 3 for mode I and II, respectively. The geometry functions f(a/W) for the respective fracture geometries in mode I and II with a respective notch geometry are further explained in the following chapters. When the load reaches a critical load F_c, fracture occurs and K_I becomes K_{Iq}, the conditional fracture toughness. The size requirement according to ASTM standard E399 [34] can be fulfilled due to the brittleness of the interfaces and the small plastic zone size. The fracture toughness is called "conditional" because the notch is introduced by FIB milling instead of fatigue pre-loading and is not atomically sharp. Hence, only K_{Iq} instead of K_{Ic} values are given in the following.

The bending stress at the surface of unotched micro-cantilevers is evaluated by means of linear-elastic Euler-Bernoulli beam theory of clamped beams with regular rectangular cross sections in the case of small displacements:

$$\sigma_{bending} = \frac{6FL}{BW^2} \tag{3}$$

Again, the critical load at failure is used to calculate the bending strength for mode I. Shear stresses in respective unnotched specimens are determined by the following equation:

$$\tau = \frac{F}{AW} \tag{4}$$

Where A is the total curved area of the PyC layer in the two shear regions assigned to each shear specimen. Critical shear loads upon failure of the first shear surface are used for the determination of the shear strength.

3. Finite element modeling

FE models of the specimen geometries (STN and CN) for mode I and mode II loading are implemented in the commercial implicit solver Abaqus/Standard (Dassault Systems, USA) to analyze the stress intensity
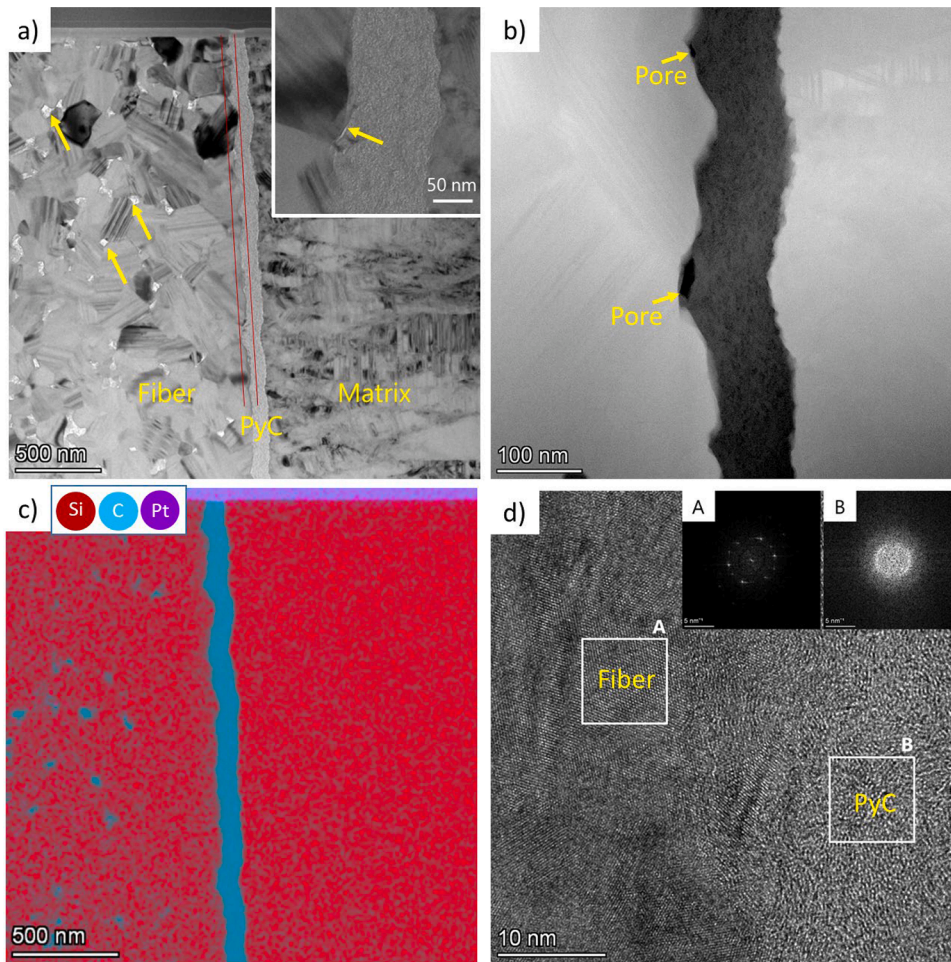
Fig. 2. a) Bright field TEM image showing the microstructure of the fiber, PyC interlayer and matrix. Arrows highlight the precipitates at the fiber grain boundaries and the inset at higher magnification indicates a flaw along the fiber/PyC interface. Two red lines illustrate the width of the roughness profile. b) Dark field TEM image of the interface structure showing two nano-sized pores. c) STEM-EDS mapping shows the chemical distribution of C and Si across the interface shown in a). Carbon-rich precipitates at fiber grain boundaries are visible. d) HRTEM at the interface highlighting the amorphous feature of PyC. Insets in d) show exemplary local fast Fourier transform (FFT) of region A from SiC fiber and Region B from PyC interphase.
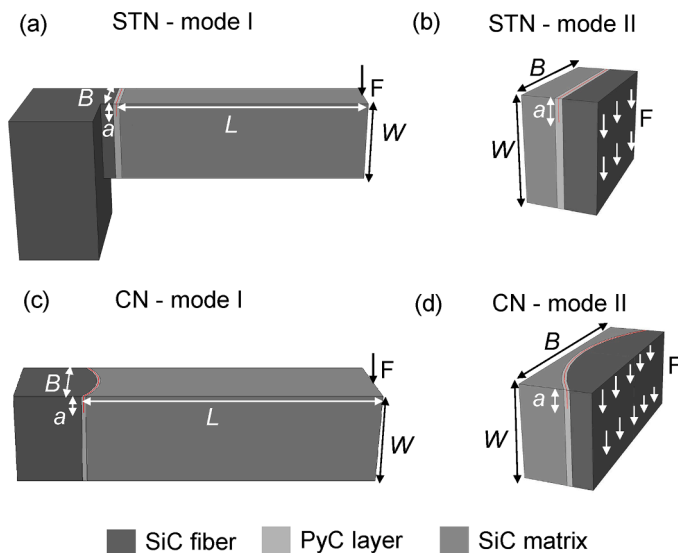
Fig. 3. FE models for (a) STN – mode I, (b) STN – mode II, (c) CN – mode I and (d) CN – mode II. The dimensions and load points are labelled. The pre-crack marked in red is located at the central plane of the PyC layer.

factors for initial notch placement in the PyC interlayer. For mode II, only the sheared portion of the specimen is modeled explicitly and simple shear boundary conditions are applied. The four different models are shown schematically in Fig. 3, which also labels the corresponding

dimensions. Note that for mode I of curved notch type, the length L is measured at the edge. The linear-elastic material behavior of the SiC/PyC/SiC system is modeled using an isotropic stiffness tensor, specifically $E_{SiC\text{-}fiber} = 366$ GPa, $\nu_{SiC\text{-}fiber} = 0.21$, $E_{SiC\text{-}matrix} = 538$ GPa, $\nu_{SiC\text{-}matrix} = 0.21$. For the elastic properties of PyC layer, a variety of Young's moduli ($E_{PyC} = 25 - 45$ GPa, $\nu_{PyC} = 0.22$) are applied, as the elastic modulus of PyC changes with different factors, for instance, the pyrolysis temperature, the holding time of pyrolysis, the testing technique and the testing orientation [27,35–39]. In this work, it remains challenging to experimentally measure the elastic modulus of this pyrolytic layer due to the limited thickness. That is why we use a range of literature values to investigate the influence of the PyC layer stiffness on the fracture behavior and the robustness of the developed geometry function. Notches are introduced into the model using seam cracks, which are always located at the central plane of the PyC interlayer, as marked by red lines in Fig. 3. A $\frac{1}{\sqrt{r}}$ stress singularity is introduced at the crack tip by collapsing the neighboring quadratic hexahedral elements into wedges and positioning their mid nodes at a quarter of the element length. The rest of the model is meshed with 8-node linear bricks (C3D8R) to reduce the computing time after confirming a negligible difference in average stress intensity factor compared to quadratic hexahedra (C3D20R). The stress field around the notch is assessed using the contour integral method and five contour integrals are evaluated to approximate the stress intensity factors. Parameter study on PyC elastic properties, PyC interlayer thickness and beam thickness W is performed using Python scripting, thus minimizing inconsistencies caused by manual repeated model construction as well as computation time. In this way, a suitable equation relating the stress intensity factor with these

parameters and a constant geometry factor function is determined.

4. Results

4.1. Stress intensity factor and geometry function

FE simulations are performed in four cases, STN geometry under mode I loading, STN under mode II, CN under mode I and CN under mode II. Fig. 4 shows the distribution of stress intensity factors across the beam width B. The K value at each node point across the width B is obtained by averaging over five J integral contour values. Even though only mode I and mode II loading are of interest in the present study, it is important to analyze all three fracture modes, including mode III. Only if it can be shown that only one stress intensity factor is predominant with respect to the two remaining ones, this model is suitable for testing in the predominant mode. It is therefore important to see that K_{III} is negligible with respect to K_I or K_{II} for the respective testing geometries. For mode I loading, the stress intensity factor K_I is almost constant over the width B for the STN beams and remains predominant compared with K_{II} and K_{III} [32]. By contrast, CN cantilevers under mode I loading, in spite of K_I dominance at the central part, show a mixed mode stress intensity factor when approaching the edges (Fig. 4c). To facilitate comparison, all stress intensity factor data in Fig. 4 are normalized by the average K_I in case of mode I and by the average K_{II} for mode II. From Fig. 4b) and d), both the STN and CN geometry under mode II loading has K_{II} as the dominant stress intensity factor over the whole specimen width, although K_{II} exhibits a slight variation for the CN cantilever. To calculate geometry functions for the four cases, the average of K_I in mode I loading and K_{II} in mode II loading is applied.

Compared with cantilever simulations of one homogeneous material

with well-defined elastic properties, more care needs to be taken for the current SiC-PyC-SiC sandwich system when correlating the stress intensity factor with the geometry function. Owing to the efficiency of scripting, a series of simulations with varying parameters were performed. The results show that, if using the conventional relations as shown in Eqs. (1) and (2), a consistent geometry function cannot be obtained for different PyC thicknesses t_{PyC}, PyC elastic modulus E_{PyC} and beam thickness W.

Fig. 5a and c show variations of geometry function in the case of a curved notch and different geometry parameters. Note that the K value for each geometry is calculated as the average across the sample width B, excluding the two outer nodes at each free surface. By applying Eq. (1) for geometry function in mode I (Fig. 5a), and Eq. (2) in mode II (Fig. 5c), $f_{K_I,CN}\left(\frac{a}{W}\right)$ and $f_{K_{II},CN}\left(\frac{a}{W}\right)$ do not converge to one expression for different parameter sets. In particular, there is a significant influence of the PyC layer thickness on the geometry function. While keeping the other variables constant, a difference over 20% in geometry factor is evident when comparing the model with 50 nm and 200 nm PyC layer, even reaching 30% in mode II (Fig. 5a and c). This implies that if the same geometry function $f_{K_I,CN}\left(\frac{a}{W}\right)$ and $f_{K_{II},CN}\left(\frac{a}{W}\right)$ is applied on cantilevers of different t, E_{PyC} and W, a significant error can occur during the calculation of stress intensity factors from experiments. In order to have a convergent expression at various parameters, a normalised geometry function $\widetilde{f}$ is put forward for this particular material system, which takes t, E_{PyC} and W into account, as seen from the insets in Fig. 4b and d. The new formula in mode I $\widetilde{f}_{K_I,CN}\left(\frac{a}{W}\right)$ and $\widetilde{f}_{K_{II},CN}\left(\frac{a}{W}\right)$ in mode II converges decently, which largely reduces the largest relative difference to approximately 5% (Fig. 5b and d). Further, by taking the average at each
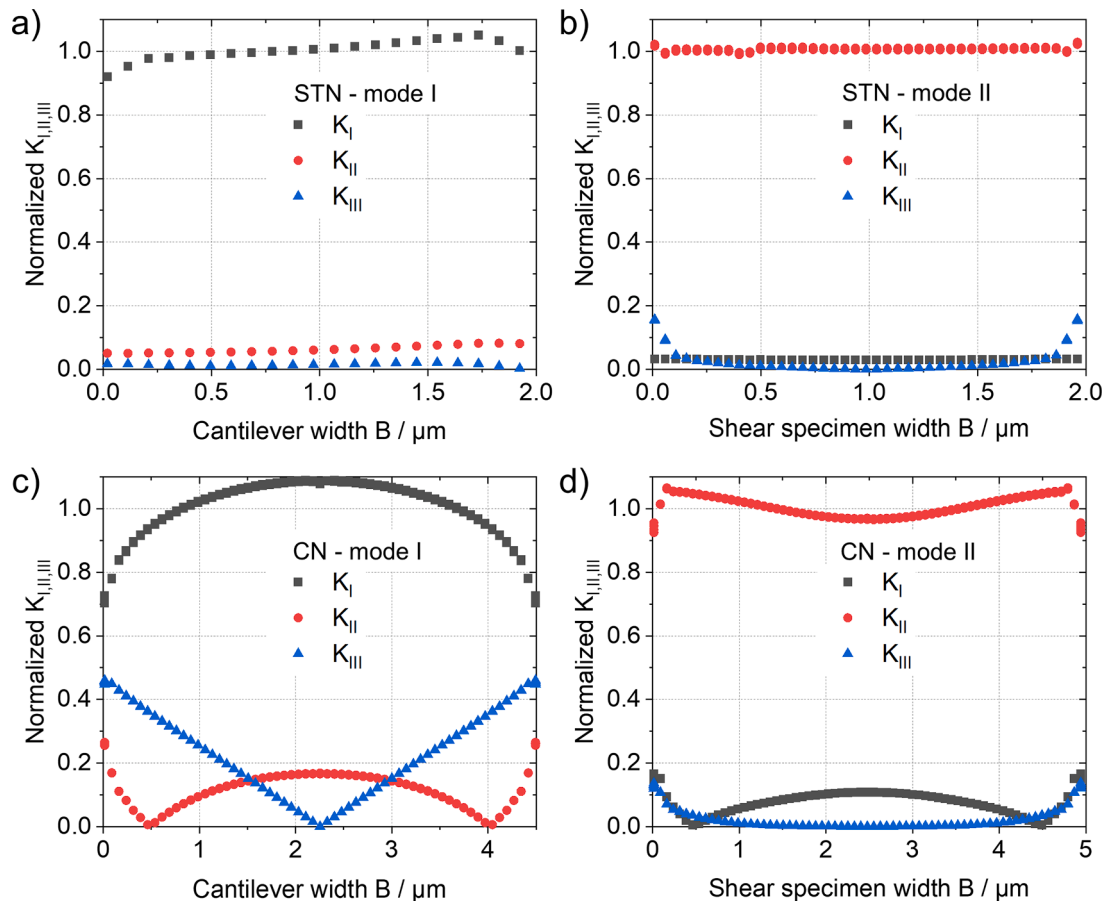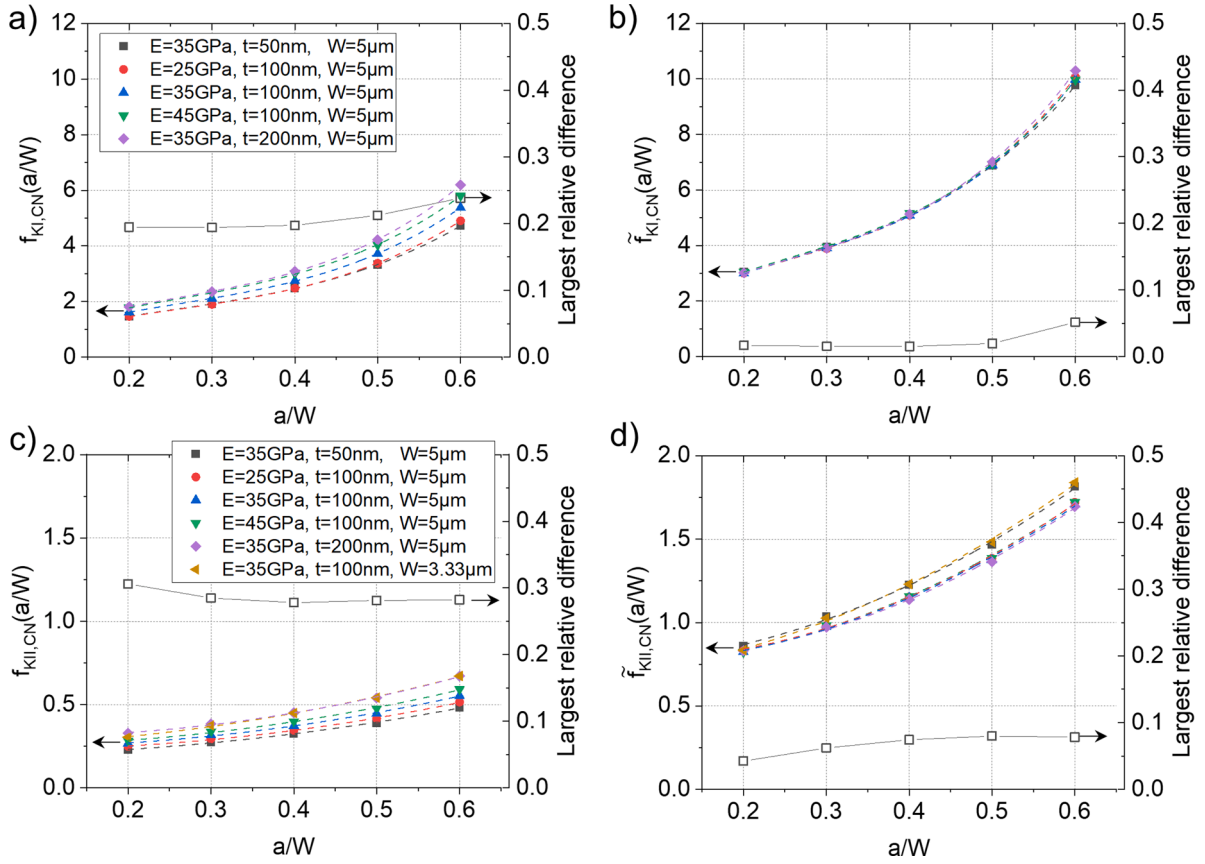

Fig. 4. Normalized stress intensity factor profiles over the specimen width B for (a) STN mode I, (b) STN mode II, (c) CN mode I and (d) CN mode II. Data is obtained from models with E_{PyC} = 35 GPa, PyC thickness of 100 nm and a/W = 0.2.

Fig. 5. (a) and (c) Dimensionless geometry functions f in the case of curved notches (CN) and applying specific PyC thicknesses, PyC elastic moduli and specimen thicknesses for mode I (micro-cantilevers) and mode II (micro-shear), respectively. In (b) and (d) normalized expressions are proposed for mode I and II, respectively, resulting in both cases in much lower errors for a given a/W ratio as expressed to the right of each graph by the "largest relative difference". A value of 35 GPa is chosen for E_0.

a/W ratio, a unified $\widetilde{f}_{K_{I,CN}}\left(\frac{a}{W}\right)$ and $\widetilde{f}_{K_{II,CN}}\left(\frac{a}{W}\right)$ can be described in a third-order and second-order polynomial function, respectively, which can increase the accuracy of the calculated stress intensity factor. Normalised geometry functions are given in Eqs. (5) and (6) for the curved notch configuration:

$$\widetilde{f}_{K_{I,CN}}\left(\frac{a}{W}\right) = 81.353x^3 - 61.994x^2 + 24.782x - 0.112 \tag{5}$$

$$\widetilde{f}_{K_{II,CN}}\left(\frac{a}{W}\right) = 2.930x^2 - 0.098x + 0.745 \tag{6}$$

Accordingly, the equations to calculate the stress intensity factor in mode I and in mode II for the curved notches are given as:

$$K_{I,CN} = \frac{FL}{BW^{3/2}}\widetilde{f}_{K_{I,CN}}\left(\frac{a}{W}\right)\cdot\left(\frac{E}{E_0}\right)^{0.304}\cdot\left(\frac{t}{W}\right)^{0.158} \tag{7}$$

$$K_{II,CN} = \frac{F}{2B\sqrt{W}}\widetilde{f}_{K_{II,CN}}\left(\frac{a}{W}\right)\cdot\left(\frac{E}{E_0}\right)^{0.234}\cdot\left(\frac{t}{W}\right)^{0.288} \tag{8}$$

Analogously, for the STN geometries, normalised geometry functions are given in Eqs. (9) and (10):

$$\widetilde{f}_{K_{I,STN}}\left(\frac{a}{W}\right) = 144.54x^3 - 109.206x^2 + 41.335x - 0.511 \tag{9}$$

$$\widetilde{f}_{K_{II,STN}}\left(\frac{a}{W}\right) = 3.324x^2 + 0.401x + 0.850 \tag{10}$$

The corresponding stress intensity factors are written in Eqs. (11) and (12):

$$K_{I,STN} = \frac{FL}{BW^{3/2}}\widetilde{f}_{K_{I,STN}}\left(\frac{a}{W}\right)\cdot\left(\frac{E}{E_0}\right)^{0.222}\cdot\left(\frac{t}{W}\right)^{0.260} \tag{11}$$

$$K_{II,STN} = \frac{F}{2B\sqrt{W}}\widetilde{f}_{K_{II,STN}}\left(\frac{a}{W}\right)\cdot\left(\frac{E}{E_0}\right)^{0.169}\cdot\left(\frac{t}{W}\right)^{0.326} \tag{12}$$

The reader is referred to supplementary Figure S1 for more details on the STN geometry and geometry function evaluation. A validity check has been performed for a variety of parameters for both modes and notch configurations and an overview is given in Table 2. In the following experimental results, the calculation of the stress intensity factors always uses the experimentally measured PyC interlayer thickness t and geometry thicknesses W, B while assuming a constant value for $E_{PyC} = 35$ GPa.

4.2. Interface fracture toughness

Whenever the sphero-conical indentation tip is used, the displacement is corrected for the elastic-plastic indentation of the tip. This is

Table 2
Range of simulated geometric dimensions to verify and ensure the robustness of the geometry functions. Note as well that the validated a/W ratio is only between 0.2 - 0.6.

Parameter	mode 1, CN	mode 2, CN	mode 1, STN	mode 2, STN
W / μm	2.5 - 10	2.5 - 6	1.5 - 3.5	1.0 - 3.0
B/W	0.5 - 2.0	0.83 - 2.0	0.6 - 1.3	0.7 - 2.0
t_{PyC} / nm	50 - 200	50 - 200	50 - 200	50 - 200
E_{PyC} / GPa	25 - 45	25 - 45	25 - 45	25 - 45

done for all tests with the exception of STN cantilevers with extremely low failure loads of below 0.1 mN. Here, no indentation marks are observed on the specimen surface after testing. For the displacement correction, we performed indentations with the same tip in embedded fibers and measured the load-displacement signal. From the fit of the loading part, a displacement correction is obtained and applied to the micro-scale experiments. However, a displacement correction does not influence the determination of stress intensity factor or strength, as only the applied failure load is required for the analysis.

Load-displacement data of STN micro-cantilevers are shown in Fig. 6a-c. Since notch length to specimen height ratios of about 0.35–0.45 are applied for those specimens and since the failure is highly brittle, very low critical loads just below 0.1 mN are measured upon failure. As can be seen in the corresponding SE images the local weakness consists of the inside interface between fiber and PyC. Fracture surfaces feature the flakes of the carbon interlayer and it can be noted that the curved fiber geometry makes an ideal STN specimen preparation by FIB impossible and the notch length deviates toward the cantilever backside for the presented test piece. This backside is not observable during FIB milling and complicates the process for this specimen type. These problems can be overcome by using curved notches.

The fracture behavior of micro-cantilevers with CN are shown in Fig. 6d. Again, representative specimens are chosen, for which normalized geometry functions as given in Eq. (5) are applied. After the initial linear-elastic loading section up to critical loads in the range of approximately 0.6–0.8 mN, which are used for the calculation of the fracture toughness, a short but characteristic force plateau is seen at a bending displacement of 80–150 nm.

This plateau is assumed to be linked with a gradual lateral extension of the first initiated crack at the center towards the edge of the specimen. The crack initiates first at the SiC_{fiber}/PyC interface at the center of the specimen as this location has the largest driving force and since the SiC_{fiber}/PyC interface is sufficiently weak. Once initiated at the site with highest stress intensity, the crack propagates laterally along the fiber/PyC interface until it reaches the free edge. We hypothesize that no significant vertical movement (Δa) is taking place during this phase due to the lack of force drop. This plateau might be also related with the adaption between the crack front by FIB milling and the location of weak interface that fails. After this plateau stage, the load drops quite clearly to a load level of ~0.4 mN, followed by slow stable crack growth with a more or less constant reduction of force with bending displacement. This initial sharp load drop can be correlated with a slightly different fracture behavior. The crack morphology at the lateral cantilever surfaces, where a mixed mode stress state is present (see Fig. 4c), differs in all tests from the one in the center with predominant plane strain state. Videos recorded during the in-situ tests, (see supplementary material) show that fracture initiation occurs non-homogeneously over the width of the specimen: At the free surfaces, the crack forms inside the SiC matrix but near the PyC interlayer (see Fig. 6g), while in the central part of the cantilever the crack propagates along the PyC/SiC fiber interface (see Fig. 6h and i). The weaker site is found to be consistently throughout the tests the interface between PyC layer and SiC fiber.

Load-displacement data of micro-shear specimens with STN design are depicted in Fig. 7a-d. The variation of critical loads for the four different tests, originates from a more complex milling procedure leading to slightly larger variations in geometry than for the simpler cantilever geometry. The loading is not strictly linear since small plastic imprints are formed by the conical indentation tip centrally on the shear specimen surface leading to a nonlinearity in the loading curve. Once a critical load value is reached, finite load drops are observed, which depend on the alignment of the straight FIB notch to the interlayer. Pure shearing in mode II leads initially to an abrupt instable crack propagation along the SiC_{fiber}/PyC interface, which is higher for specimens with
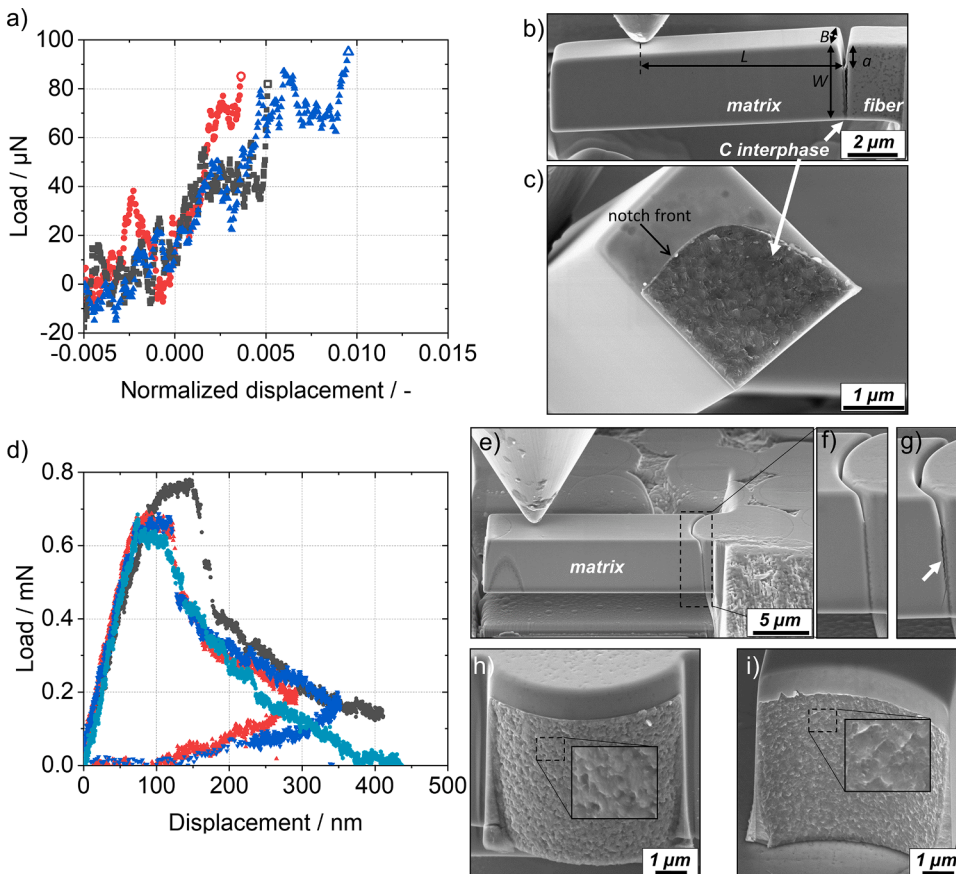

Fig. 6. a) Load-displacement data for three micro-cantilevers with STN geometry, b) SE image of fractured cantilever showing fracture at the inside interface fiber-PyC and c) SE image of an inclined fracture surface showing the microstructure of the carbon interphase and the irregular notch front. d) Load-displacement data of micro-cantilevers with curved-notches, e) and f) SE images of a cantilever before testing, g) after testing with fracture near the PyC phase and h) and i) SE images of fracture surfaces of the remaining fiber and cantilever side, respectively. In-situ videos for these two cases can be found in the supplementary material.
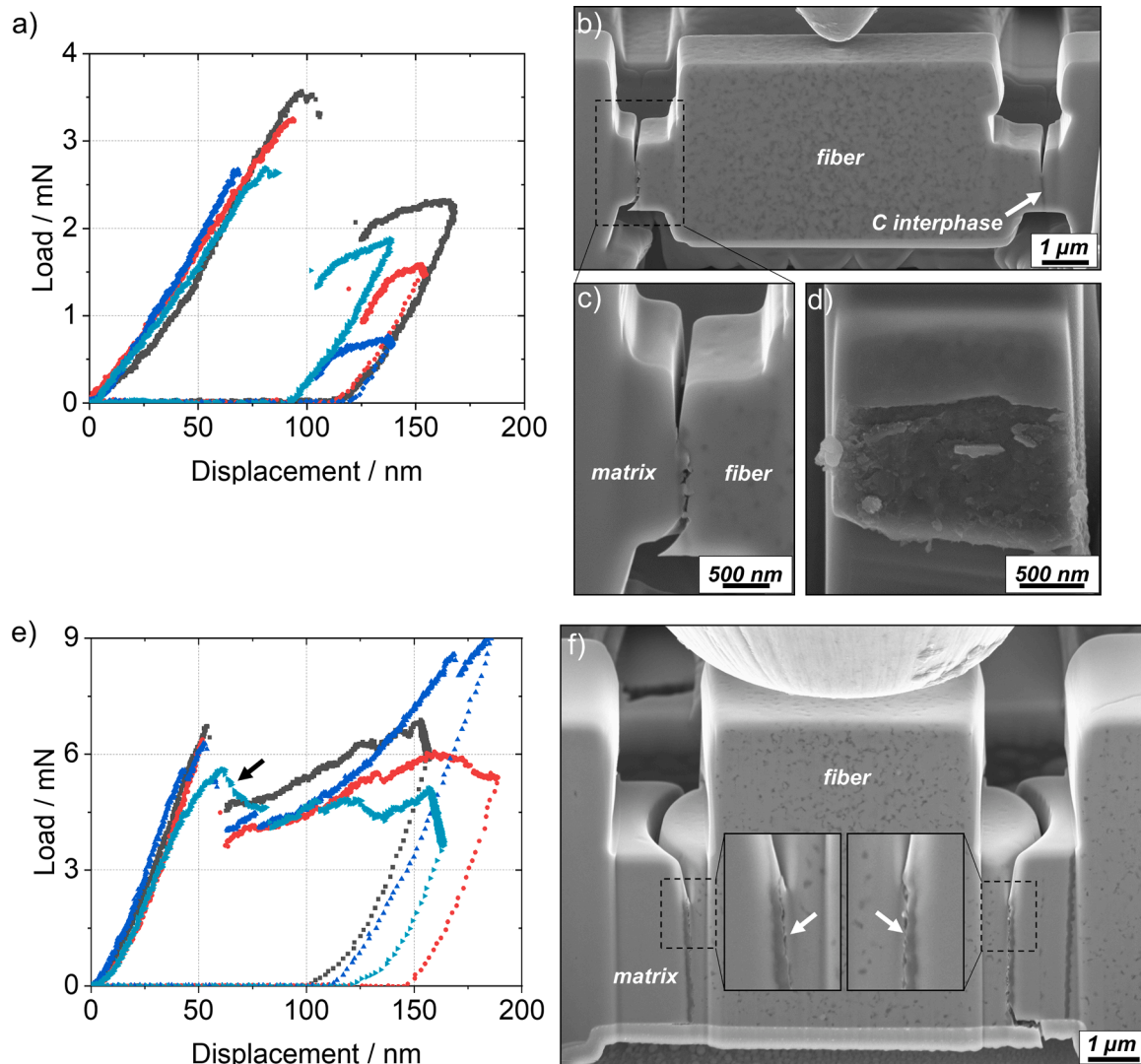
Fig. 7. a) Load-displacement data of micro-shear specimens with STN notch, b-d) SE images of a sheared specimen showing fracture at the left side and a rough fracture surface of the left matrix support side due to significant wear during shearing. e) Load-displacement data of micro-shear specimens with CN geometry and f) SE image of a shear specimen after testing showing first fracture at the right shear side followed by fracture at the left side at both times the inside interface between SiC fiber and PyC as highlighted by the magnified views. In-situ videos for these two cases can be found in the supplementary material.

a larger critical load. In this case and depending on the sample size, more elastic energy is stored and can, once it is released, contribute to the creation of larger fracture surfaces. This mode II fracture happens always either on the left or the right side as a function of local FIB preparation differences as well as slight loading asymmetries. Once fracture is stabilized further loading is a kind of bending since the second shear zone with notch remains intact until final unloading. Just as seen before for mode I loading, fracture is observed at the interface between PyC and SiC fiber.

Similar shear tests to the ones described in the previous section are performed on specimens featuring curved notches. Those tests are shown in Fig. 7e-f. This is done to better align the notch to the curved interlayers, which then also allows the design of specimens with more ideal aspect ratios in terms of width and height as a function of fiber diameter. With straight notches, specimens need to be very thin (small *B*). Load levels are generally higher than for mode II shear specimens compared with for STN because specimens are wider but the scatter between specimens is very low and shear fracture behavior is very reproducible. The major difference is that a kind of overloading because of a too significant mismatch between FIB notch and interface can be avoided much more easily. In one case stable fracture is even observed

as depicted by an arrow in Fig. 7e. In the other cases the load drop after reaching a critical load occurred far less instable than for the STN design. As can be seen in Fig. 7f, fracture in those specimens always occurs at the interface between SiC fiber and PyC. Fracture surface analysis could not be performed for these specimens because of the complexity in removing the sheared specimens with curved shear edges from the bulk material without severely altering the originally formed fracture surfaces.

4.3. Adhesive interface strength

To investigate the tensile strength of the interlayer in the absence of FIB prepared notches, unnotched micro-cantilever bending experiments are performed (Fig. 8a). A linear elastic loading behavior up to the point of brittle fracture of the SiC-PyC interface at low bending displacements just under 200 nm is observable. SE images in Fig. 8b and c demonstrate the brittle fracture process, which occurs mainly at the inside interface (centrally in the cantilever). At the free surfaces to the left and right side, the fracture path crosses the interlayer, which goes along with a change in stress state towards the surfaces and the outside interface is partially visible. This is in line with FE results shown in Fig. 4c, where K_{III} becomes significant at the free surfaces. A bending strength of 934 ± 137
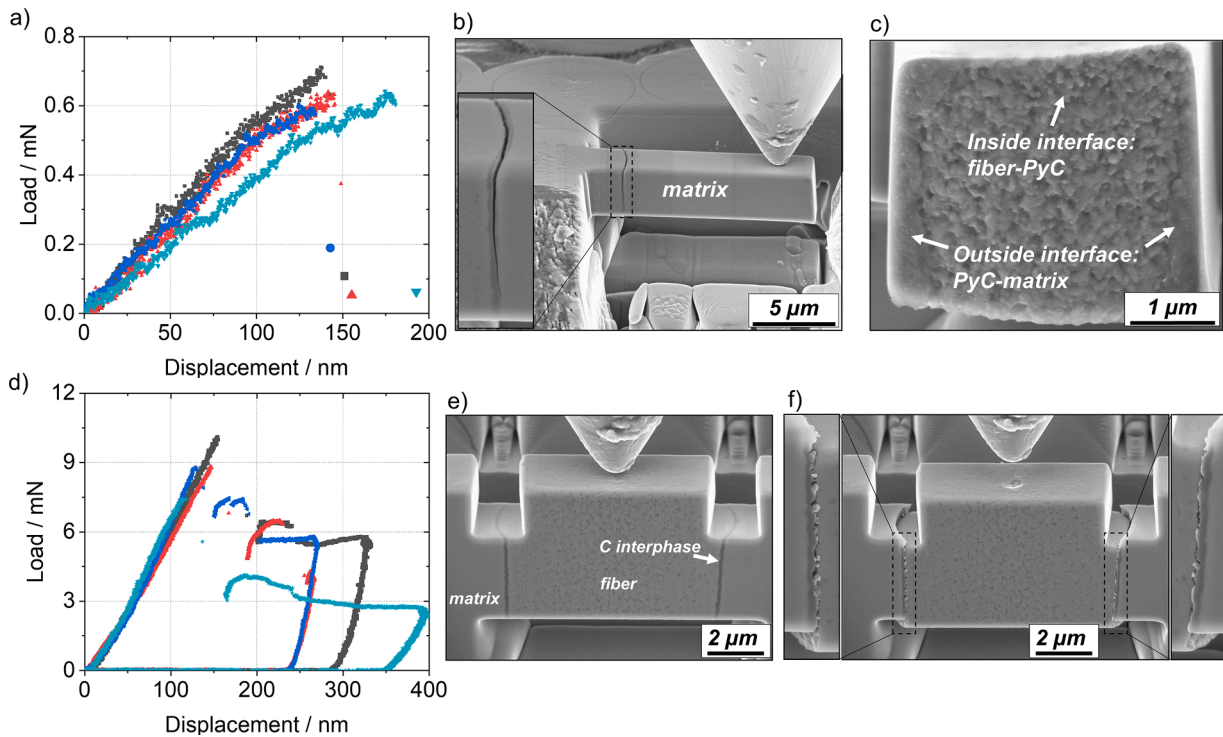
Fig. 8. a) Load-displacement data of unnotched micro-cantilevers, b) SE images of a specimen after testing showing fracture at the PyC interphase and c) SE image of the fracture surface of the support (fiber side) indicating failure mainly along the inside interphase between fiber and PyC. d) Load-displacement data of unnotched micro-shear specimens, e) SE image of a specimen before and f) after testing. Magnified views of the left and right shear faces demonstrate that failure takes place at the interface between fiber and PyC. In-situ videos for these two cases can be found in the supplementary material.

MPa is determined.

Similar to the micro-cantilevers, shear strength testing is performed using unnotched micro-shear specimens as shown in Fig. 8d-f. In all cases, one shear side fails at significantly higher loads than for the previously shown cases at the inside interface, as depicted in Fig. 8f. The second shear face fails shortly after the first one and a second load drop is noticed. During progressive shearing of the specimen, the load does not drop to zero because of frictional forces between the crack faces but remains at a more or less constant load level before final unloading. Critical shear strength values of 418 ± 36 MPa are measured.

5. Discussion

5.1. Micro-scale fracture properties

In Fig. 9, mechanical data for all geometries is presented. Interfacial fracture toughness (K_I and K_{II}) under mode I and mode II is shown for the notched specimens. The adhesive strength at failure for samples without a notch is given as well with "B" denoting bending and "S" shear. Regarding the fracture toughness, for the STN notch type the scatter is much larger compared to the CN type even though the same number of tests is performed. This is clearly because of the lack in precision when tailoring a straight notch to a curved interlayer of the round fiber and the necessity to prepare particularly thin specimens. As a consequence, imperfections in the preparation process, as can be seen in the cantilever notch profile in Fig. 6c exemplarily, not only lead to larger scatter but also to a general overestimation of fracture toughness. This overestimation is caused by the additional surface energy needed to drive the crack over the distance between the root of the FIB prepared notch and the weak interface between the PyC layer at the SiC fiber, at which crack propagation preferably takes place. For STN specimens, $K_{i,q}$ of 0.26 ± 0.14 MPa$\sqrt{m}$ and 0.34 ± 0.09 MPa$\sqrt{m}$ are determined under mode I and mode II loading, respectively.

CN specimens reveal an even lower fracture toughness with $0.24 \pm$
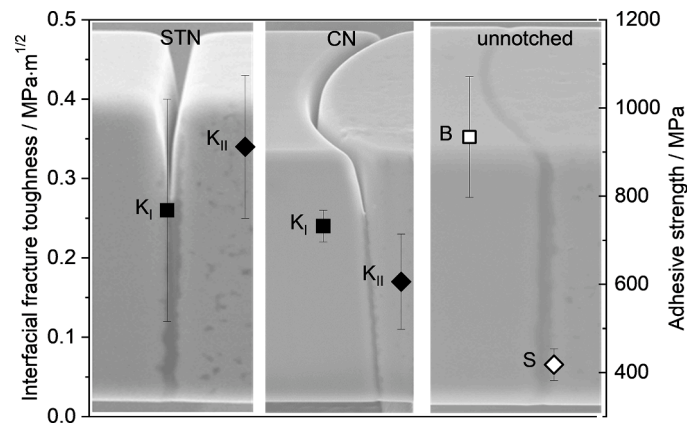
Fig. 9. (Filled symbols) Interfacial fracture toughness under mode I (K_I) and mode II (K_{II}) loading for the two notched configurations STN and CN. (Open symbols) Adhesive strength from bending and shearing tests without notches. Bend and shear geometries are marked as "B" and "S", respectively.

0.02 MPa$\sqrt{m}$ and 0.17 ± 0.06 MPa$\sqrt{m}$ for mode I and mode II, respectively. The slightly larger scatter for mode II is partly caused by averaging of geometric dimensions for the left and right shear faces, which differ due to FIB imperfections. After optimizing the notch geometry into a curved one, the interfacial fracture toughness now reveals a lower value for mode II than for mode I. This shows the importance of appropriate notch design to adequately measure fracture toughness in particular when measuring the micromechanical properties of complexly shaped interfaces. Similar microscale trends in interfacial toughness have been reported for the adhesive fracture between BN/SiC fiber based on microscale double cantilever beam and push out tests [28].

Since the proper calculation of fracture toughness involves several

different variables, an error propagation analysis is performed on the load F, geometry dimensions W, B, L, a, PyC thickness t and Young's modulus E. The uncertainty in load ΔF is taken as 10 μN based on the noise data of the load cell and in all dimensions taken as 100 nm according to the SEM measurement. The uncertainty of the thickness of the PyC layer, Δt, is considered as the standard deviation of the measurements in the respective tested geometries and is in the range of 10 to 20 nm. The elastic modulus of the PyC layer has an uncertainty ΔE of 20 GPa. These uncertainties consequently deliver an uncertainty of 0.06 MPa$\sqrt{m}$ for $K_{I,STN}$, 0.07 MPa$\sqrt{m}$ for $K_{II,STN}$, 0.05 MPa$\sqrt{m}$ for $K_{I,CN}$ and 0.03 MPa$\sqrt{m}$ for $K_{II,CN}$, which are in a similar range to the experimental data scatter.

The trend with lower fracture toughness in mode II is confirmed by unnotched specimens. Whereas the unnotched micro-cantilevers sustain average bending stresses up to 934 ± 137 MPa, shear specimens fail at about half of this value at 418 ± 36 MPa. Though a large scatter in the adhesive shear strength of SiC composites is reported, ranging from 35 MPa to 600 MPa (overwhelmingly evaluated by single fiber push-out tests with sample thickness in the order of 100 μm) [40–42], the value obtained in this work is in fact comparable to the literature work (~350 MPa), if taking into account the PyC interlayer thickness about 100 nm and the polycrystalline feature of SiC fibers [41].

With a known fracture strength and the fracture toughness, the order of magnitude of the critical flaw sizes in the interlayer can be approximated using Griffith's equation:

$$K_{Ic} = \sigma_f \sqrt{\pi a} \tag{13}$$

Where σ_f is the fracture strength of unnotched specimens and it is noted that K_{Iq} instead of K_{Ic} is used here. Using the experimental results of CN micro-cantilevers, critical flaw sizes on the order of 20 nm are calculated, which seem reasonable when relating them to fracture surfaces and the flake structure of the interphase layer, see Fig. 6c, exemplarily. From TEM analysis, shown in Fig. 2b, small pores of nanometer size were also observed along the SiC$_{fiber}$/PyC interface.

Noteworthy as well is that our work delivers a significantly lower interface fracture resistance of the PyC/SiC fiber system (compare with K_I ~0.8 MPa$\sqrt{m}$ in [27]). In the current investigated SiC$_{fiber}$/PyC/SiC$_{matrix}$ system, the microstructural features are in fact well comparable to those in [27] and are presumably not contributing immensely to the difference in measured fracture toughness. What matters further and more critically is the consideration of the PyC thickness, its elastic modulus and elastic heterogeneity across the beam into the calculation of fracture toughness. As evident in Fig. 5a and c, a scatter of 30% in the stress intensity factor can be easily expected when changing the interlayer thickness from 50 nm to 200 nm. But considering a similar thickness of 100 nm in [27], the thickness factor cannot fully explain the big discrepancy. If we do not account for the elastic heterogeneity of the tested beams, the geometry factor for a homogenous material is almost three times higher compared to what we determine in this study by numerical simulations for our complex sandwich structure. As an example, for a/W = 0.2, Matoy et al. [43] calculated a geometry factor of 5.0 for homogeneous beams. For the same notch ratio, the geometry factor of the studied SiC$_{fiber}$/PyC/SiC$_{matrix}$ system is determined to be 1.9 for the STN Mode I (assuming PyC layer thickness of 100 nm and PyC elastic modulus of 35 GPa, for details see supplementary information). If we use a geometry factor for a homogeneous beam to interpret our force-displacement data, the mode I fracture toughness would increase from 0.26 ± 0.14 MPa$\sqrt{m}$ to approximately 0.78 MPa$\sqrt{m}$, which lies in the same range as earlier studies of similar CMCs [27]. This shows that extreme care has to be taken when interpreting experimental data of such interface systems, as the use of a geometry factor for homogeneous beams results in a significant overestimation of the fracture toughness. This aspect needs to be carefully addressed when dealing with heterogeneous systems, especially since the impact of systematic errors on the individual parameters,

as discussed above, is rather low. Finally, also the shape of the interlayer and therefore the geometric choice and precision of the notch milling are crucial. As seen from Fig. 9 and the STN case an overestimation of the fracture toughness is found when additional elastic energy is needed for the creation of new surfaces to overcome the distance between notch root and preferred fracture location. This overestimation is found for both bending and shear specimens.

5.2. Fracture path

For the discussion of the observed fracture path, which is found to follow the interface between SiC fiber and PyC layer, there are two aspects to consider. First, the initial crack notch is targeted to be located in the center of the PyC layer. However, the crack deviates always to the SiC$_{fiber}$/PyC interface instead of remaining in the PyC layer or deviating towards the PyC/SiC$_{matrix}$ interface. Second, once the crack has deviated to the SiC$_{fiber}$/PyC interface, it propagates further along the interfacial path without kinking out into the SiC fiber or to the PyC phase.

To support the discussion, we convert the stress intensity factor K to the interfacial energy release rate G following Eqs. (14)–(16) [44] and also calculate the Dundurs parameters (α, β) assuming a plane strain condition:

$$G = \frac{(1 - \beta^2)}{E_*} K^2 \tag{14}$$

$$\frac{1}{E_*} = \frac{1}{2} \left(\frac{1 - \nu_1^2}{E_1} + \frac{1 - \nu_2^2}{E_2} \right) \tag{15}$$

$$\beta = \frac{1}{2} \cdot \frac{\mu_1(1 - 2\nu_2) - \mu_2(1 - 2\nu_1)}{\mu_1(1 - \nu_2) + \mu_2(1 - \nu_1)} \tag{16}$$

$$\alpha = \frac{\mu_1(1 - \nu_2) - \mu_2(1 - \nu_1)}{\mu_1(1 - \nu_2) + \mu_2(1 - \nu_1)} \tag{17}$$

Above as input, E_1 and E_2 denote the elastic moduli of SiC fiber and PyC layer, K the SiC$_{fiber}$/PyC interface toughness, ν_1 and ν_2 the respective Poisson's ratio while μ_1 and μ_2 are the corresponding shear moduli. The Dundurs parameter α equals 0.82 and β 0.30. After conversion, the stress intensity factors lead to interfacial energy release rates of G_I^c 0.78 ± 0.01 J/m^2 and G_{II}^c 0.39 ± 0.05 J/m^2 for the CN configuration. Those values are significantly lower than the ones reported for SiC fibers (~ 10 J/m^2) [27,28], and for the pyrolytic interphase (~ 50 J/m^2) [45].

The ideal crack propagation angle can be predicted from FE based on the maximum energy release rate criterion (G^{max}), as shown in the supplementary Figure S2 and Table S1. A negative angle corresponds to crack propagation pointed towards the SiC$_{fiber}$/PyC layer interface, a positive value towards the PyC/SiC$_{matrix}$ interface. For mode II both in STN and CN configurations, if the crack propagation criterion is chosen such that it propagates in the direction of maximum energy release rate G^{max}, this promotes a crack deflection towards fiber side. In contrast, for mode 1 in STN and partially in CN geometry, the simulation based on G^{max} predicts initial crack propagation towards the PyC/SiC$_{matrix}$ interface, which is not in line with our experimental observation. Assuming that the crack first deflects to the PyC/SiC$_{matix}$ under the largest energy release rate, the further propagation of this crack along the PyC/SiC$_{matix}$ can be instable due to its higher toughness. This could cause the crack to kink out through the PyC layer, following the less tough SiC$_{fiber}$/PyC interface as experimentally measured (G_I^c 0.78 ± 0.01 J/m^2, G_{II}^c 0.39 ± 0.05 J/m^2). This phenomenon of the crack path switching from one interface to the other has been reported for other tri-material systems [46,47]. However, this possible fast switching process can be hardly captured due to the limited thickness of interlayer and the roughness of interfaces.

Lopes Fernandez et al. [46] investigate comparably thick but very compliant interlayers in a tri-material system. For sufficiently long

cracks and important stiffness variations in their composite structure, their experiments and simulations show that the crack deflects from the center of the compliant phase towards the interface near the side with larger elastic modulus. We see a similar deflection from the compliant PyC towards an interface, however, close to the less stiff side. The difference suggests that the specific interfacial fracture toughness has a significant influence on the crack deflection as well, as detailed below.

The significantly low interfacial toughness of the SiC_{fiber}/PyC interface ensures the continuous propagation along the SiC_{fiber}/PyC interface without kinking out to either side. Crack kinking depends on the ratio k between the interface toughness and the fracture toughness of dissimilar counterparts (here SiC fiber and PyC). Comparing G_I^c 0.78 ± 0.01 J/m^2 and G_{II}^c 0.39 ± 0.05 J/m^2 of SiC_{fiber}/PyC interface with 6~8 J/m^2 of SiC fiber [28], and 28~48 J/m^2 of PyC interlayer [45], the ratio k falls into the range of 0.02~0.1 (G_I^c used for a conservative estimation). By taking into account the elastic mismatch (Dundurs' parameter α 0.75, comparable to 0.82 in this work) as well as the mode mixity $\tan^{-1}(K_{II}/K_I)$, previous researchers deduced a criterion, that predicts whether or not stable interfacial crack propagation without kinking is possible [48]. This criterion predicts interfacial failure in our system.

Hence, it is only the SiC fiber/PyC interface toughness, which is measured in our micro-scale configurations. The preference of crack propagation at the SiC_{fiber}/PyC interface, compared to PyC /SiC_{matrix} interface, is supposedly attributed to the larger roughness of the fiber surfaces (see TEM analysis in Fig. 2) that are introduced during the preparation processes such as sintering and densification at high temperatures up to 1800 ℃ [49].

5.3. Correlation of local with global fracture behavior in composites

In CFMC materials, sufficiently weak interfaces between fiber and matrix are desired to deflect cracks along the long interfaces instead of directly penetrating into fibers, effectively toughening the composites [50]. In the current system, the SiC fiber/PyC interface exhibits an interfacial toughness as low as 0.39 ± 0.05 J/m^2 (in Mode II) and acts as the preferred location for crack propagation. However, while it is critical to have a sufficiently high fracture resistance, too weak interfaces might not be able to properly transfer load between fiber and matrix and result in unsatisfactory strength, such as the ultimate tensile strength, of the overall composite [51]. An optimized tradeoff between toughness and strength needs further investigation through a similar quantitative methodology. For instance, a numerical relation between the interface strength and interfacial fracture toughness and the roughness of the fiber surfaces as well as the interphase thickness is to be investigated [52]. Furthermore, as the CFMC materials are designed for high temperature applications, a quantification of the interfacial properties at elevated temperatures also requires future research.

6. Summary

This micro-scale fracture study has enabled a thorough mechanical analysis of SiC-PyC-SiC composite with interlayer thicknesses of just below 100 nm in mode I bending and mode II shearing. The approach applied consists on the one side of an in-depth numerical assessment of geometry functions and stress intensity factor distributions by simulating a large variety of specimen parameters and elastic properties to understand their influence on the fracture process. In a second step, simulation results are directly applied to micro-mechanical bending and shear geometries prepared on individual fibers.

It is found that in the present case an appropriate curved notch design and precise FIB milling is indispensable for the analysis of fracture behavior of complexly shaped interfaces and to determine fracture toughness data, which are as low as 0.24 ± 0.02 MPa$\sqrt{m}$ and 0.17 ± 0.06 MPa$\sqrt{m}$ for mode I and II, respectively. In case of the less aligned straight through notches (STN), a small but systematic overestimation of

fracture toughness for both loading modes is found. Furthermore, data scatter is increased due to misalignment of notch and interlayer as well as the difficulties in determining the crack length. In both cases, bending and shearing, fracture takes place at the interface between PyC and SiC fiber as the weak spot, whereas the opposite interface between PyC and SiC matrix is found to be always resistant to fracture. Mode-mixity, as has been numerically found close to free surfaces of micro-cantilevers with curved notches, produces a change in fracture behavior at the lateral specimen surfaces with the crack locally deflecting into the matrix with little effect on measured fracture toughness. Micro-mechanical tests on unnotched specimens show the same fracture paths, underline the specific weakness of the SiC_{fiber}/PyC interface and provide fracture stresses for bending of up to 934 ± 137 MPa (mode I) and for shear of 418 ± 36 MPa (mode II). Using those results and the previously determined fracture toughness, critical flaw sizes in the interlayer of 20 nm can be approximated, which is approximately the pore size along the SiC_{fiber}/PyC interface.

Even though an interlayer generally needs to be well characterized analytically prior to mechanical testing, this study is translatable to further primarily brittle CFMC systems or composite structures. For this, an adaptation of interlayer thickness, specimen dimensions and elastic properties is required to allow a thorough mechanical characterization of the specimen. These tests may be an important input for (thermo-) mechanical simulation of large composite structures taking into consideration the fiber orientation and density as well as flaw distribution.

Declaration of Competing Interest

The authors declare that they have no known competing financial interests or personal relationships that could have appeared to influence the work reported in this paper.

Acknowledgements

Supplementary materials

Supplementary material associated with this article can be found, in the online version, at doi:10.1016/j.actamat.2023.119273.

References

[1] W.A. Curtin, Theory of mechanical properties of ceramic-matrix composites, J. Am. Ceram. Soc. 74 (1991) 2837–2845, https://doi.org/10.1111/j.1151-2916.1991. tb06852.x.

[2] I.W. Donald, P.W. McMillan, Ceramic-matrix composites, J. Mater. Sci. 11 (1976) 949–972, https://doi.org/10.1007/BF00542312.

[3] Q. An, J. Chen, W. Ming, M. Chen, Machining of SiC ceramic matrix composites: a review, Chin. J. Aeronaut. 34 (2021) 540–567, https://doi.org/10.1016/j. cja.2020.08.001.

[4] J. Sun, D. Ye, J. Zou, X. Chen, Y. Wang, J. Yuan, H. Liang, H. Qu, J. Binner, J. Bai, A review on additive manufacturing of ceramic matrix composites, J. Mater. Sci. Technol. 138 (2023) 1–16, https://doi.org/10.1016/j.jmst.2022.06.039.

[5] N. Radhika, M. Sathish, A review on Si-based ceramic matrix composites and their infiltration based techniques, Silicon 14 (2022) 10141–10171, https://doi.org/ 10.1007/s12633-022-01763-y.

[6] N. Carrère, E. Martin, J. Lamon, The influence of the interphase and associated interfaces on the deflection of matrix cracks in ceramic matrix composites, Compos. Part Appl. Sci. Manuf. 31 (2000) 1179–1190, https://doi.org/10.1016/ S1359-835X(00)00095-6.

[7] G. Fantozzi, P. Reynaud, Mechanical hysteresis in ceramic matrix composites, Mater. Sci. Eng. A. 521–522 (2009) 18–23, https://doi.org/10.1016/j. msea.2008.09.128.

[8] F. Hild, A. Burr, F.A. Leckie, Matrix cracking and debonding of ceramic-matrix composites, Int. J. Solids Struct. 33 (1996) 1209–1220, https://doi.org/10.1016/ 0020-7683(95)00067-4.

[9] R.C. Robinson, J.L. Smialek, SiC recession caused by SiO_2 scale volatility under combustion conditions: I, experimental results and empirical model, J. Am. Ceram. Soc. 82 (1999) 1817–1825, https://doi.org/10.1111/j.1151-2916.1999.tb02004.x.

[10] M.J. Walock, V. Heng, A. Nieto, A. Ghoshal, M. Murugan, D. Driemeyer, Ceramic matrix composite materials for engine exhaust systems on next-generation vertical lift vehicles, J. Eng. Gas Turbines Power. 140 (2018), https://doi.org/10.1115/1.4040011.

[11] Y. Katoh, L.L. Snead, Silicon carbide and its composites for nuclear applications – historical overview, J. Nucl. Mater. 526 (2019), 151849, https://doi.org/10.1016/j.jnucmat.2019.151849.

[12] V. Angelici Avincola, K. Fitzgerald, D. Shepherd, D. Kinay, C. Sauder, M. Steinbrueck, High-temperature tests of silicon carbide composite cladding under GFR conditions, Energy Procedia 127 (2017) 320–328, https://doi.org/10.1016/j.egypro.2017.08.116.

[13] K.A. Terrani, C. Ang, L.L. Snead, Y. Katoh, Irradiation stability and thermo-mechanical properties of NITE-SiC irradiated to 10 dpa, J. Nucl. Mater. 499 (2018) 242–247, https://doi.org/10.1016/j.jnucmat.2017.11.040.

[14] A.S. Argon, Fracture of composites, in: H. Herman (Ed.), Treatise Mater. Sci. Technol., Elsevier, 1972, pp. 79–114, https://doi.org/10.1016/B978-0-12-341801-2.50007-2.

[15] H. Yu, X. Zhou, W. Zhang, H. Peng, C. Zhang, Influence of SiC coating thickness on mechanical properties of SiCf/SiC composite, J. Nucl. Mater. 442 (2013) 53–59, https://doi.org/10.1016/j.jnucmat.2013.08.018.

[16] R. Naslain, O. Dugne, A. Guette, J. Sevely, C.R. Brosse, J.-P. Rocher, J. Cotteret, Boron nitride interphase in ceramic-matrix composites, J. Am. Ceram. Soc. 74 (1991) 2482–2488, https://doi.org/10.1111/j.1151-2916.1991.tb06789.x.

[17] R.M.G. De Meyere, L. Gale, S. Harris, I.M. Edmonds, T.J. Marrow, D.E. J. Armstrong, Optimizing the fiber push-out method to evaluate interfacial failure in SiC/BN/SiC ceramic matrix composites, J. Am. Ceram. Soc. 104 (2021) 2741–2752, https://doi.org/10.1111/jace.17673.

[18] J. Kabel, Y. Yang, M. Balooch, C. Howard, T. Koyanagi, K.A. Terrani, Y. Katoh, P. Hosemann, Micro-mechanical evaluation of SiC-SiC composite interphase properties and debond mechanisms, Compos. Part B Eng. 131 (2017) 173–183, https://doi.org/10.1016/j.compositesb.2017.07.035.

[19] J. Kabel, T.E.J. Edwards, C. Hain, T. Kochetkova, D. Parkison, J. Michler, P. Hosemann, A novel fiber-fretting test for tribological characterization of the fiber/matrix interface, Compos. Part B Eng. 206 (2021), 108535, https://doi.org/10.1016/j.compositesb.2020.108535.

[20] W.M. Mueller, J. Moosburger-Will, M.G.R. Sause, S. Horn, Microscopic analysis of single-fiber push-out tests on ceramic matrix composites performed with Berkovich and flat-end indenter and evaluation of interfacial fracture toughness, J. Eur. Ceram. Soc. 33 (2013) 441–451, https://doi.org/10.1016/j.jeurceramsoc.2012.09.009.

[21] A. Hussey, R. De Meyere, C. Deck, D.E.J. Armstrong, Y. Zayachuk, Statistically sound application of fiber push-out method for the study of locally non-uniform interfacial properties of SiC-SiC fiber composites, J. Eur. Ceram. Soc. 40 (2020) 1052–1056, https://doi.org/10.1016/j.jeurceramsoc.2019.11.041.

[22] O.G. Diaz, K. Marquardt, S. Harris, L. Gale, L. Vandeperre, E. Saiz, F. Giuliani, Degradation mechanisms of SiC/BN/SiC after low temperature humidity exposure, J. Eur. Ceram. Soc. 40 (2020) 3863–3874, https://doi.org/10.1016/j.jeurceramsoc.2020.05.007.

[23] E. Buet, C. Sauder, D. Sornin, S. Poissonnet, J.-N. Rouzaud, C. Vix-Guterl, Influence of surface fibre properties and textural organization of a pyrocarbon interphase on the interfacial shear stress of SiC/SiC minicomposites reinforced with Hi-Nicalon S and Tyranno SA3 fibres, J. Eur. Ceram. Soc. 34 (2014) 179–188, https://doi.org/10.1016/j.jeurceramsoc.2013.08.027.

[24] O. Karakoc, T. Koyanagi, T. Nozawa, Y. Katoh, Fiber/matrix debonding evaluation of SiC/SiC composites using micropillar compression technique, Compos. Part B Eng. 224 (2021), 109189, https://doi.org/10.1016/j.compositesb.2021.109189.

[25] J. Kabel, P. Hosemann, Y. Zayachuk, D.E.J. Armstrong, T. Koyanagi, Y. Katoh, C. Deck, Ceramic composites: a review of toughening mechanisms and demonstration of micropillar compression for interface property extraction, J. Mater. Res. 33 (2018) 424–439, https://doi.org/10.1557/jmr.2017.473.

[26] D. Frazer, M.D. Abad, D. Krumwiede, C.A. Back, H.E. Khalifa, C.P. Deck, P. Hosemann, Localized mechanical property assessment of SiC/SiC composite materials, Compos. Part Appl. Sci. Manuf. 70 (2015) 93–101, https://doi.org/10.1016/j.compositesa.2014.11.008.

[27] Y. Zayachuk, P. Karamched, C. Deck, P. Hosemann, D.E.J. Armstrong, Linking microstructure and local mechanical properties in SiC-SiC fiber composite using micromechanical testing, Acta Mater 168 (2019) 178–189, https://doi.org/10.1016/j.actamat.2019.02.001.

[28] O. Gavalda-Diaz, R. Manno, A. Melro, G. Allegri, S.R. Hallett, L. Vandeperre, E. Saiz, F. Giuliani, Mode I and Mode II interfacial fracture energy of SiC/BN/SiC CMCs, Acta Mater 215 (2021), 117125, https://doi.org/10.1016/j.actamat.2021.117125.

[29] J. Ast, J.J. Schwiedrzik, N. Rohbeck, X. Maeder, J. Michler, Novel micro-scale specimens for mode-dependent fracture testing of brittle materials: a case study on GaAs single crystals, Mater. Des. 193 (2020), 108765, https://doi.org/10.1016/j.matdes.2020.108765.

[30] C.P. Deck, H.E. Khalifa, B. Sammuli, T. Hilsabeck, C.A. Back, Fabrication of SiC–SiC composites for fuel cladding in advanced reactor designs, Prog. Nucl. Energy. 57 (2012) 38–45, https://doi.org/10.1016/j.pnucene.2011.10.002.

[31] J. Ast, B. Matthey, P. Herre, S. Höhn, M. Herrmann, S.H. Christiansen, Micro-cantilever testing of diamond - silicon carbide interfaces in silicon carbide bonded diamond materials produced by reactive silicon infiltration, Open Ceram 8 (2021), 100176, https://doi.org/10.1016/j.oceram.2021.100176.

[32] J. Ast, J.J. Schwiedrzik, J. Wehrs, D. Frey, M.N. Polyakov, J. Michler, X. Maeder, The brittle-ductile transition of tungsten single crystals at the micro-scale, Mater. Des. 152 (2018) 168–180, https://doi.org/10.1016/j.matdes.2018.04.009.

[33] J. Ast, M. Ghidelli, K. Durst, M. Göken, M. Sebastiani, A.M. Korsunsky, A review of experimental approaches to fracture toughness evaluation at the micro-scale, Mater. Des. 173 (2019), 107762, https://doi.org/10.1016/j.matdes.2019.107762.

[34] ASTM International, ASTM E399-90 Standard Test Method for Plane-Strain Fracture Toughness of Metallic Materials, 1997. West Conshohocken, PA, USA.

[35] J.L. Kaae, Effect of irradiation on the mechanical properties of isotropic pyrolytic carbons, J. Nucl. Mater. 46 (1973) 121–133, https://doi.org/10.1016/0022-3115(73)90130-X.

[36] E. Rossi, J. Bauer, M. Sebastiani, Humidity-dependent flaw sensitivity in the crack propagation resistance of 3D-printed nano-ceramics, Scr. Mater. 194 (2021), 113684, https://doi.org/10.1016/j.scriptamat.2020.113684.

[37] X. He, J. Song, H. Xia, J. Tan, B. Zhang, Z. He, X. Zhou, Z. Zhu, M. Zhao, X. Liu, L. Xu, S. Bai, Direct characterization of ion implanted pyrolytic carbon coatings deposited from natural gas, Carbon N Y 68 (2014) 95–103, https://doi.org/10.1016/j.carbon.2013.10.058.

[38] B. Farbos, J.-P.Da Costa, G.L. Vignoles, J.-M. Leyssale, Nanoscale elasticity of highly anisotropic pyrocarbons, Carbon N Y 94 (2015) 285–294, https://doi.org/10.1016/j.carbon.2015.06.060.

[39] X. Zhang, L. Zhong, A. Mateos, A. Kudo, A. Vyatskikh, H. Gao, J.R. Greer, X. Li, Theoretical strength and rubber-like behaviour in micro-sized pyrolytic carbon, Nat. Nanotechnol. 14 (2019) 762–769, https://doi.org/10.1038/s41565-019-0486-y.

[40] L. Zhang, C. Ren, C. Zhou, H. Xu, X. Jin, Single fiber push-out characterization of interfacial mechanical properties in unidirectional CVI-C/SiC composites by the nano-indentation technique, Appl. Surf. Sci. 357 (2015) 1427–1433, https://doi.org/10.1016/j.apsusc.2015.10.018.

[41] W. Yang, A. Kohyama, T. Noda, Y. Katoh, T. Hinoki, H. Araki, J. Yu, Interfacial characterization of CVI-SiC/SiC composites, J. Nucl. Mater. 307–311 (2002) 1088–1092, https://doi.org/10.1016/S0022-3115(02)00949-2.

[42] H. Yu, X. Zhou, W. Zhang, H. Peng, C. Zhang, Mechanical behavior of SiCf/SiC composites with alternating PyC/SiC multilayer interphases, Mater. Des. 44 (2013) 320–324, https://doi.org/10.1016/j.matdes.2012.07.073.

[43] K. Matoy, H. Schönherr, T. Detzel, T. Schöberl, R. Pippan, C. Motz, G. Dehm, A comparative micro-cantilever study of the mechanical behavior of silicon based passivation films, Thin Solid Films 518 (2009) 247–256, https://doi.org/10.1016/j.tsf.2009.07.143.

[44] B.M. Malyshev, R.L. Salganik, The strength of adhesive joints using the theory of cracks, Int. J. Fract. Mech. 1 (1965) 114–128, https://doi.org/10.1007/BF00186749.

[45] M. Sakai, R.C. Bradt, D.B. Fischbach, Fracture toughness anisotropy of a pyrolytic carbon, J. Mater. Sci. 21 (1986) 1491–1501, https://doi.org/10.1007/BF01114701.

[46] R.Lopes Fernandes, M.K. Budzik, R. Benedictus, S. Teixeira de Freitas, Multi-material adhesive joints with thick bond-lines: crack onset and crack deflection, Compos. Struct. 266 (2021), 113687, https://doi.org/10.1016/j.compstruct.2021.113687.

[47] D. Xie, A.M. Waas, K.W. Shahwan, J.A. Schroeder, R.G. Boeman, Fracture criterion for kinking cracks in a tri-material adhesively bonded joint under mixed mode loading, Eng. Fract. Mech. 72 (2005) 2487–2504, https://doi.org/10.1016/j.engfracmech.2005.03.008.

[48] J.W. Hutchinson, Z. Suo, Mixed mode cracking in layered materials, in: J. W. Hutchinson, T.Y. Wu (Eds.), Adv. Appl. Mech., Elsevier, 1991, pp. 63–191, https://doi.org/10.1016/S0065-2156(08)70164-9.

[49] P. Wang, F. Liu, H. Wang, H. Li, Y. Gou, A review of third generation SiC fibers and SiCf/SiC composites, J. Mater. Sci. Technol. 35 (2019) 2743–2750, https://doi.org/10.1016/j.jmst.2019.07.020.

[50] X.W. Yin, L.F. Cheng, L.T. Zhang, N. Travitzky, P. Greil, Fibre-reinforced multifunctional SiC matrix composite materials, Int. Mater. Rev. 62 (2017) 117–172, https://doi.org/10.1080/09506608.2016.1213939.

[51] H. Mei, Q. Bai, Y. Sun, H. Li, H. Wang, L. Cheng, The effect of heat treatment on the strength and toughness of carbon fiber/silicon carbide composites with different pyrolytic carbon interphase thicknesses, Carbon N Y 57 (2013) 288–297, https://doi.org/10.1016/j.carbon.2013.01.076.

[52] C. Sauder, A. Brusson, J. Lamon, Influence of interface characteristics on the mechanical properties of Hi-Nicalon type-S or Tyranno-SA3 fiber-reinforced SiC/SiC Minicomposites, Int. J. Appl. Ceram. Technol. 7 (2010) 291–303, https://doi.org/10.1111/j.1744-7402.2010.02485.x.